

Defect detection and quantification in electroluminescence images of solar PV modules using U-net semantic segmentation



Lawrence Pratt ^{a, b, *}, Devashen Govender ^a, Richard Klein ^b

^a CSIR, Meiring Naude Road, Pretoria, South Africa

^b School of Computer Science and Applied Mathematics, University of the Witwatersrand, Johannesburg, South Africa

ARTICLE INFO

Article history:

Received 16 January 2021

Received in revised form

21 May 2021

Accepted 19 June 2021

Available online 25 June 2021

Keywords:

Electroluminescence

EL

PV

U-net

Semantic segmentation

Machine learning

ABSTRACT

Electroluminescence (EL) images enable defect detection in solar photovoltaic (PV) modules that are otherwise invisible to the naked eye, much the same way an x-ray enables a doctor to detect cracks and fractures in bones. The prevalence of multiple defects, e.g. micro cracks, inactive regions, gridline defects, and material defects, in PV module can be quantified with an EL image. Modern, deep learning techniques for computer vision can be applied to extract the useful information contained in the images on entire batches of PV modules. Defect detection and quantification in EL images can improve the efficiency and the reliability of PV modules both at the factory by identifying potential process issues and at the PV plant by identifying and reducing the number of faulty modules installed. In this work, we train and test a semantic segmentation model based on the u-net architecture for EL image analysis of PV modules made from mono-crystalline and multi-crystalline silicon wafer-based solar cells. This work is focused on developing and testing a deep learning method for computer vision that is independent of the equipment used to generate the EL images, independent of the wafer-based module design, and independent of the image quality.

© 2021 Elsevier Ltd. All rights reserved.

1. Introduction

Solar photovoltaic (PV) based electricity generation has increased rapidly across the world. By the end of 2019, global cumulative PV installations reached 623.2 GW (GW) [1]. By 2022, experts predict annual installations between 100 GW and 232 GW globally, depending on the growth scenario [2] and global installed capacity reaching 2840 GW by 2030 [3]. The growth of solar PV installations is largely attributable to the lower cost of electricity generated by new solar PV compared to new power plants based on other technologies.

Solar PV based electricity generation begins with the conversion of photons to electrons within the PV module. Poor quality and reliability of the PV modules will have an immediate and long-term impact on the safety, performance, and financial return on investment from the PV plant. PV modules constitute roughly 25–35% of the overall cost of utility-scale solar PV projects in the 5–100 MW range, and the module cost remains the single biggest cost item for PV systems regardless of the scale [4]. Manufacturers are under

constant pressure to deliver PV modules at lower prices, and this pressure can conflict with the needs of the consumer for a product with high quality and reliability. Independent analysis and defect detection in electroluminescence (EL) images is one means for buyers to hold manufacturers accountable for quality and reliability in a cost-competitive market.

PV modules made from crystalline silicon cells are susceptible to cracking, and cracked cells have decrease electricity generation over time [5]. Cracks form during module manufacturing, shipping, installation, and heavy stresses induced from wind, snow, and human traffic during routine operations and maintenance. EL images are widely used in the industry to detect cracks in solar PV modules. Fig. 1 shows a typical EL image of a PV module made with mono-crystalline silicon wafers. The module consists of 60 cells arranged in a 6 × 10 grid. The cells are typically connected in series with multiple interconnecting ribbons on each cell. Severely cracked cells are visible on the left side of the EL image that would not be visible during a visual inspection of the module itself.

PV modules are susceptible to other defects that can be seen in

* Corresponding author. Council for Scientific and Industrial Research (CSIR), Meiring Naude Road, Pretoria, South Africa.

E-mail address: [\(L. Pratt\).](mailto:lpratt@csir.co.za)

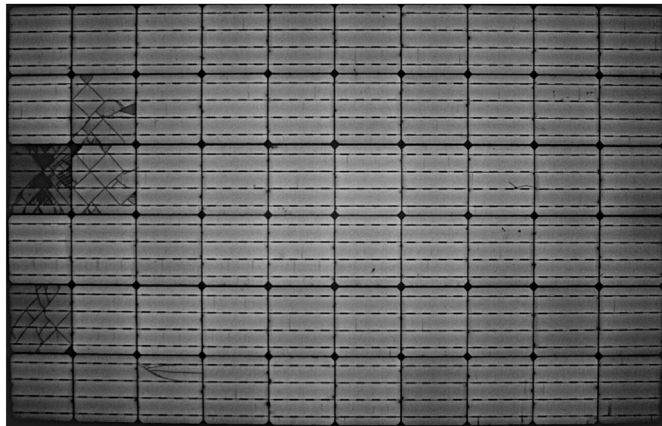


Fig. 1. EL image of a PV module made from mono-crystalline cells exhibiting cracked cells in the three left columns.

EL images. Inactive areas appear as dark, irregular shaped regions where sections of the cell are isolated from the external circuit due to cracks. Gridline defects appear as dark lines running perpendicular to the ribbon interconnections. Other defects with origins in manufacturing and environmental stress can be observed, such as belt marks, dark edges along one or two sides of the cell, corrosion along the ribbon interconnects, and dead cells.

Computer vision has proven effective to automatically identify defects in EL images of solar cells. Statistical methods, support vector machines (SVMs), and convolutional neural networks (CNNs) have been used for object detection and localization of various defect types typically focused on cracks, inactive areas, and gridline defects. Computer vision using semantic segmentation improves upon the earlier methods by generating a pixel-level classification which enables object detection, classification, and quantification of multiple defects. With pixel-level classification, PV module quality can be analyzed for statistical differences in batches from multiple suppliers of different PV modules and over time for the same batch of PV modules. This information would be useful during procurement, operations, maintenance, and warranty claims.

We present results from the application of a semantic segmentation model applied to EL images of solar PV modules for defect detection, classification, and quantification. The model was then applied to EL images taken on a batch of modules subjected to a laboratory controlled accelerated stress test sequence to produce the pixel-level defect classification masks for each module over time. The pixel-level classifications maps were then used to estimate the prevalence of each defect type by counting the pixels attributed to each defect type in each image. This article may be the first to present results using semantic segmentation for the analysis and quantification of multiple defect types captured in EL images of solar cells during an accelerated stress test sequence.

The article continues with a literature review in Section 2, an introduction to EL imaging in Section 3, methods in Section 4, results in Section 5, conclusion in Section 6, and acknowledgments in Section 7.

2. Literature review

Defect detection in optical images of bare solar cells has been the topic of several papers, including a review paper on surface defect detection on solar PV cells using computer vision techniques [6]. Specific topics on bare wafers and cells include the following: self-learning features for crack detection [7]; Particle Swarm

Optimization for crack detection [8]; SVMs for crack detection [9]; and mean-shift based defect detection for fingerprint detection [10]. While defect and crack detection on visual images of bare wafers are well suited for the production line, they are not applicable to the finished module. In a finished module, the solar cell is laminated in a stack of polymers and glass for protection against the environment, and those layers obscure the surface of the solar cell. Thus the EL images are analyzed to capture useful information from a finished PV module.

Publications on defect detection in EL images of laminated PV modules include work on image pre-processing, object detection, and defect classification. Several papers describe methods for cropping module-level EL images into component cells [11–14]. Cell level EL images are typically used in defect detection and classification pipelines rather than the full module-level images. The cell level images yield a larger training dataset because typical module images have 60 or 72 cells per modules while the smaller images are less computationally expensive to process. Other papers describe pre-processing methods such as image normalization [15] and perspective and rotation transformations [13]. Methods for defect detection and classification in EL images include: statistical methods for pixel-level crack detection [16], Random Forests (RFs) and SVMs for detection of finger defects, cracks, and inactive regions [11]; CNNs for classification of good, cracked or corroded cells [12]; CNNs for classification of solar cells with cracks, material defects, and gridline defects [17]; and SVMs and CNNs for assigning defect probabilities to single cells within a module based on the defect type [18]. Tang et al. [19] recently published a method for augmenting EL images using generative adversarial networks (GANs) to increase the number of training data available and a CNN for defect detection.

Semantic segmentation has been the topic of several publications across a range of applications. Semantic segmentation focuses the computer vision task down from labeling a region within an image to labeling each pixel within an image. The model assigns a defect class to each pixel and returns a replica of the original image colored according to the defect classification. u-net for semantic segmentation was first introduced in 2015 and evaluated on biomedical images of cell membranes [20]. The u-net model includes a series of blocks comprised of convolutional layers and max pooling layers that encode or learn the features in the image. The u-net then decodes the result from the encoder and upsamples the output to recover the original image size with pixel-level classification. Semantic segmentation has been used to evaluate road scenes [21], brain tumors [22], the cityscapes dataset [23], MRI images of the brain [24], the common objects in context (COCO) dataset [25], advanced scanning transmission electron microscopy (STEM) images of steel [26], and other datasets [27]. Zhang et al. [28] recently published a method for detecting thin cracks in images of pavement combining u-nets and GANs focused on addressing the challenges in detecting thin cracks with mostly background pixels that could prove useful in future work for crack detection optimization in EL images.

In this paper, we experiment with a semantic segmentation model for defect detection and classification in EL images of solar cells extracted with only minor pre-processing of the images. The pixel-wise classification of each solar cell enables defect detection and quantification across multiple defects at once. The quantification of defects, i.e. that raw count of pixels classified to each defect class, can be useful in analyzing data from laboratory experiments, rating quality metrics in batches of PV modules, and for plant level inspection analysis, provided the supporting EL images are available. To our knowledge, this is the first work to apply semantic segmentation techniques to EL images of PV modules for defect detection and classification.

3. EL images of PV modules

EL imaging is an effective method to detect micro-cracks in PV modules made from silicon cells [29]. The resulting image is like an x-ray, allowing the analyst to detect defects not be visible in the optical image. Micro-cracks can form during cell processing, module assembly, transportation, installation, and under stresses that occur in the field, and these cracks can negatively impact performance in the field [29]. An estimated one million final EL images are produced every day across the globe in solar PV module manufacturing facilities alone, based on 100 GW of annual production at an average of 300 W per panel.

The IEC 60904-13 technical specification describes the industry standard methods for EL image collection in the lab environment. The IEA PVPS Report T13-10:2018 also provide guidance for EL and IR imaging [30]. In summary, a DC current is forced through a PV module or string of PV modules to generate electron-hole pairs in the device, simulating the effect of the photons when the module is exposed to sunlight. A specialized camera captures the image which is then analyzed manually or automatically for defect detection and classification. In recent years, methods have been developed for collecting EL images in the daylight [31–33] and in-situ during environmental stress tests [34]. In-situ, ground-based and drone based EL imaging have been successfully implemented [35], so the volume of EL images collected on fielded modules will likely grow in the future.

Fig. 2 shows examples of cell level EL images for mono-crystalline silicon (mono-si) and multi-crystalline silicon (multi-si) cells. A mono-si cell without defects exhibits a clear surface, whereas a multi-si cell without defects exhibits irregular dark regions due to the crystalline grain boundaries, thus complicating object detection and classification on multi-si cells. These images exhibit various defects of interest: cracks, inactive regions, belt marks, horizontal gridline defects, and corroded interconnection ribbons. The images also exhibit interconnect ribbons and solder bond pads that appear as dark lines running from top to bottom, although they are not defects.

4. Methodology

Fig. 3 summarizes the methodology in three stages: pre-processing the EL images, training the model using the EL images, and predicting defects in new EL images using the model.

4.1. Pre-processing: Source the EL images

EL images were gathered from public and private sources. Cell level EL images published by ZAE Bayern¹ [36] and the Solar Durability and Lifetime Extension (SDLE) Center at Case Western Reserve University² were downloaded from the internet. Module-level EL images were provided by: 1) CFV Labs, a PV module testing and certification lab in the USA, 2) ARTsolar, a PV module manufacturer in South Africa, and 3) the CSIR, a research institution in South Africa. The EL images were assigned unique IDs and organized in a structured directory tree.

4.2. Pre-processing: Create the cell level images

The module-level EL images were cropped to extract the solar cell level images as the basic unit of analysis, following the lead of previous authors [11,12,16–18]. The EL images were cropped using

a custom python function based on the PeakUtils library. **Fig. 4** shows a module-level EL image and the corresponding profiles for average intensities of pixels along the rows and columns which correspond to the x,y coordinates for cell spaces. The intersection of the peaks corresponds to the four corners of each cell in the module-level image. In this example, the lesser peaks along the columns correspond to the ribbon interconnects.

During the cropping process, the cell level images were expanded to include the half-cells that surround each full cell. The authors chose to extend beyond the cell borders for two reasons. First, the method creates training images that include the spaces between the cells which can be used by the model to detect mono-si versus multi-si cell types. Mono-si wafers are cut from round ingots that form ‘pseudo-squares’ with rounded corners which create a diamond shape feature in the space where cell ‘corners’ converge while multi-si wafers are cut from rectangular ingots to form squares with 90° corners which do not create the diamond shape. Second, the additional buffer ensures that the solar cell at the center is fully visible and not clipped off at one or more edges, as sometimes occurs when cropping just the one cell. **Fig. 5** shows examples of the resulting cell-level EL images. All the images from ZAE Bayern and the SDLE include artificial padding on all four sides since only the cell level images were available. Module-level EL images from ARTsolar, CFV Labs, and CSIR were cropped to include surrounding cells and/or padding for edge and corner cells. After cropping and padding, each cell level image shows a full cell in the center, regardless of the source.

Finally, all the cell images were resized and recoded. The EL images and the corresponding ground truth masks were resized to 512 pixels x 512 pixels so that the images input to the model are consistent, regardless of the source. The ground truth masks were then recoded so that each pixel was assigned a unique number from 0 to 23, corresponding to the feature or defect.

4.3. Pre-processing: Create the ground truth masks using GIMP

The ground truth masks represent the ‘true’ defect classification for each pixel in the EL image. The ground truth masks together with the corresponding EL images form the critical pairs needed for training, testing, and validation of the model. The ground truth masks were generated by manually coloring a copy of the corresponding EL images so that the color of each pixel corresponds to a specific defect or feature in the corresponding EL image. A team of individuals from the CSIR, Wits University, and the public were trained to color the EL images in GIMP 2.10.14 [37] according to the prescribed color code.

Fig. 6 shows the ground truth masks for the corresponding EL images shown above in **Fig. 5**. Each pixel in the ground truth masks was classified as one of twelve (12) intrinsic features or eleven (11) extrinsic defects by a human and colored accordingly. The features and defects are listed as the labels in **Fig. 7** (a) and **Fig. 7** (b), respectively. The intrinsic features of the cell consist of the regions that are part of the solar module by design, for example, spacing between cells, the ribbon interconnects, bus bars, and module borders. The extrinsic defects include cracks, inactive regions, belt mark defects, gridline defects, and corrosion. The padded regions were colored olive and any pixels not identified as one of the features or defects was colored black.

Fig. 7 shows the distribution of the features and defects encoded in the ground truth mask. Due to the multi-classification nature of this experiment, the effective size of the ground truth dataset is greater than the total number of images because each image is counted multiple times, once for each feature and defect in the image. The subsequent analysis focuses on detecting the cracks,

¹ <https://github.com/zae-bayern/elpv-dataset/tree/master/images>.

² <https://osf.io/4qrtv/>.

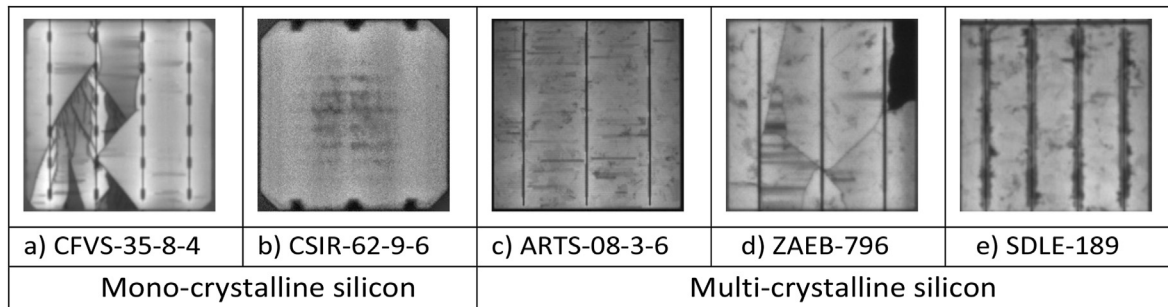


Fig. 2. A selection of EL images from mono-si and multi-si with a) cracks and inactive regions, b) belt mark defects, c) gridline defects, d) cracks and inactive regions, and e) corrosion along the ribbon interconnects.

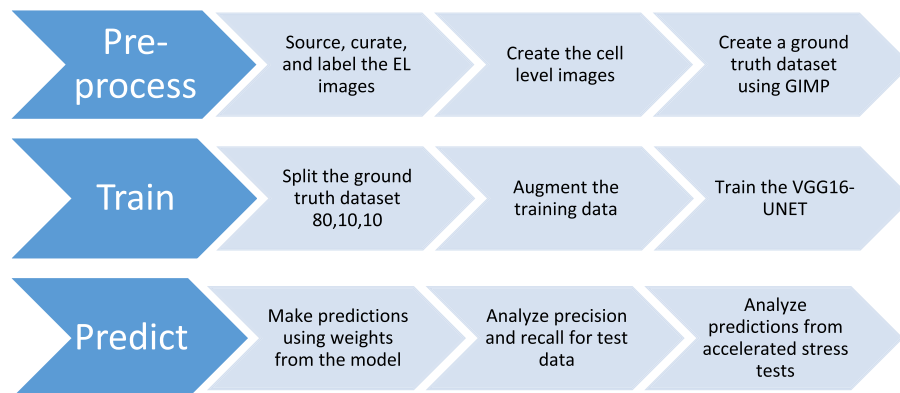


Fig. 3. Three-stage methodology: pre-processing the EL images, training the model using the EL images, and predicting defects in new EL images using the model.

gridline, and inactive defects, as the sample size for the remaining defect types is still small.

4.4. Training: Create the training, validation, and test datasets

The cell level EL images and corresponding ground truth masks were divided into three separate datasets: the training and validation datasets are used during model training, and the test dataset is used to measure the accuracy of the final model. Each dataset consists of selected EL images and the corresponding ground truth masks. First, the test dataset was created from thirty (30) cells randomly selected from all the available cells with cracks or inactive regions so that the subsequent analysis could focus on these key defects in sufficient numbers. Next, the remaining cells were randomly assigned to the training and validation datasets. Of the 148 cell images with ground truth masks, 108 (73%) were assigned to training, 10 (7%) were assigned to validation, and 30 (20%) were assigned to test.

After creating the three datasets, the training images and masks were augmented. Augmentation refers to a standard practice in machine learning that takes the original image and creates many similar images so that the training dataset can be increased in a meaningful and useful way. In this experiment, each training image and corresponding ground truth mask was augmented using a horizontal flip, a vertical flip, and 180° rotation. Fig. 8 shows a sequence of images for one representative cell from the training dataset, including the original ground truth mask, resized, recoded, and augmented. The augmentation occurred only after the split to avoid any cross-contamination, i.e., none of the augmented images from the training dataset appeared in the validation or test datasets. Each EL image and corresponding ground truth mask yielded a

total of four images and masks for training. The validation and test sets were not augmented.

4.5. Training: Train the u-net model

The u-net model for semantic segmentation was adapted for EL images starting with computer code published by Gupta [38]. The model implements a VGG-16 base model (encoder) and a U-NET semantic segmentation model (decoder), with over 12 million parameters to be learned, i.e. optimized to reduce the errors in the predictions. The details of the u-net model are left to the reader, as they go beyond the scope of this article. Once trained on EL images, the model can analyze a new EL image and predict the most likely classification for each pixel in the EL image, without any human interpretation. The model was trained on the EL images and corresponding ground truth masks in the training dataset, using pre-trained weights from ImageNet dataset as a starting point for the parameters in the model.

5. Experimental results and discussion

5.1. Test Dataset

The test dataset consisted of thirty (30) EL images with at least some cracks or inactive areas. The test images were input to the trained model and the model generated thirty (30) prediction masks, one for each EL image. The prediction mask is a colored map corresponding to the test image showing the model's best guess for each pixel classification. The prediction map looks like a ground truth mask, except that the prediction mask was generated from the model and the ground truth mask was generated manually. The

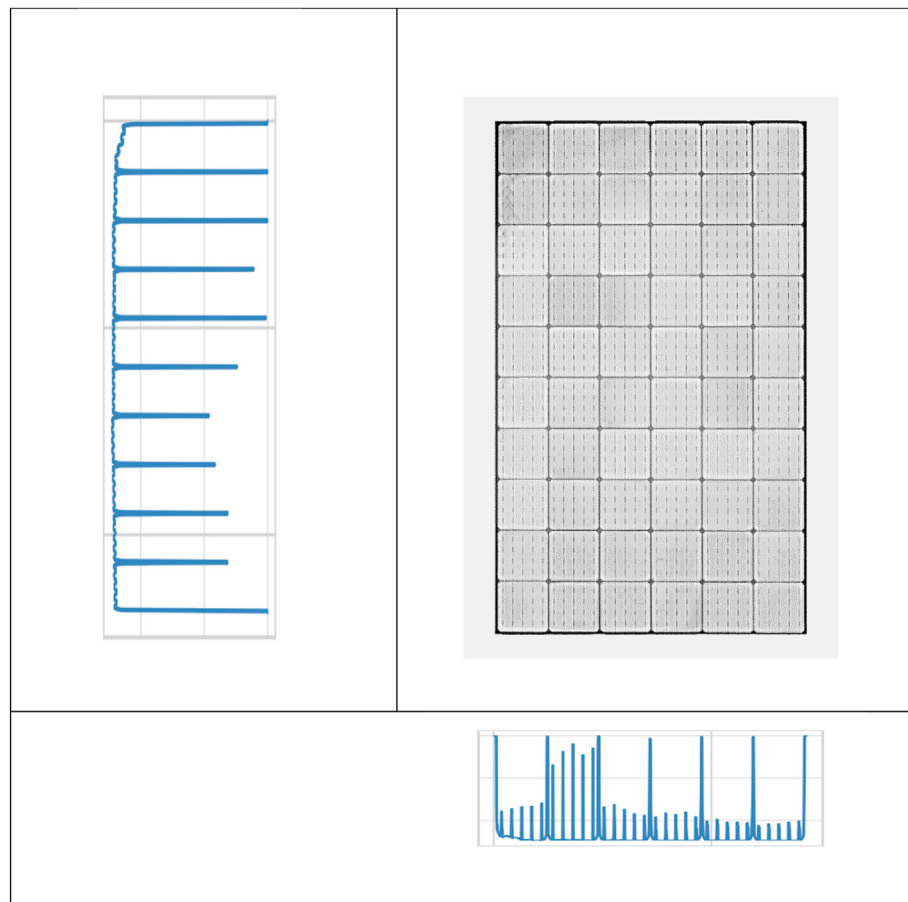


Fig. 4. Profiles created from the row-wise and column-wise average intensities with peaks corresponding to cell spacing regions of the full module image.

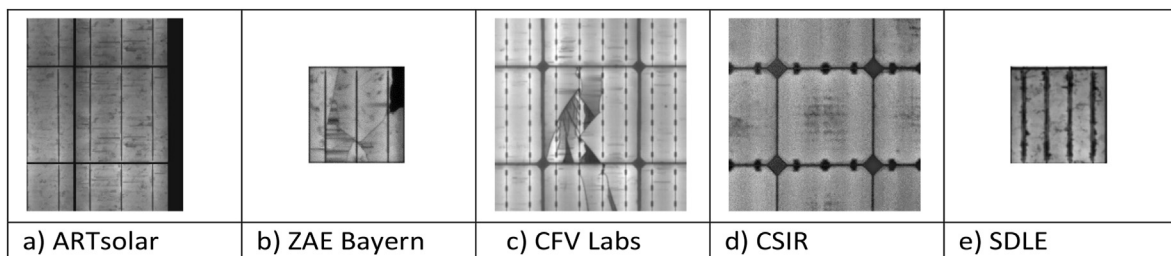


Fig. 5. Examples of cell level EL images, one from each source: a) ARTsolar multi-si cell cropped from the edge of a full module, b) ZAE Bayern single multi-si cell with padding on four sides, c) CFV Labs mono-si cell cropped from the center of a full module, d) CSIR mono-si cell cropped from the center of a full module, and e) SDLE single multi-si cell with padding on four sides.

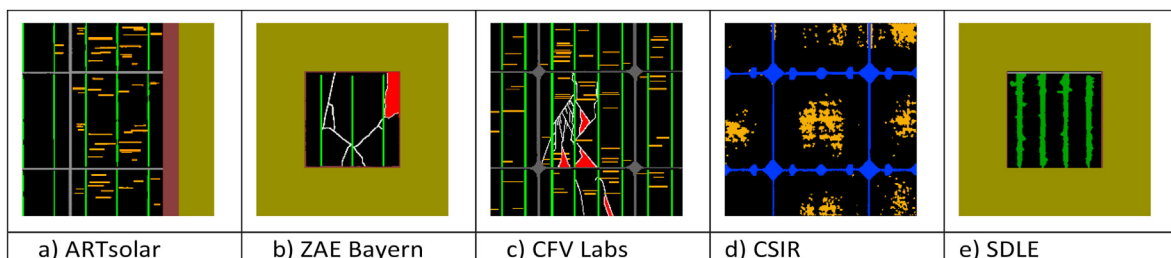


Fig. 6. Examples of ground truth masks showing pixels colored according to prescribed values: green for interconnect ribbons (a,b,c); brown for module edge (a); white for cracks (b,c); red for inactive areas (b,c); golden rod for belt marks (d); blue for dogbone spacing (d); orange for gridline defects (a,c); olive for padding (a, b,e); dark green for corroded interconnects (e); and black for background (a,b,c,d,e).

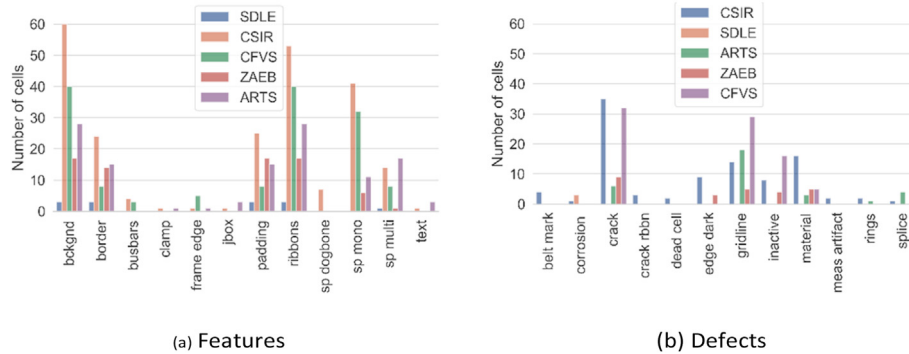


Fig. 7. Distribution of pixel classifications by source, grouped by (a) intrinsic features and (b) extrinsic defects.

comparison between the computer-generated prediction mask and the manual ground truth mask for the test dataset follows in this section, beginning with a summary graph of all the cells and then drilling down to specific regions of specific cells. The analysis focuses specifically on four common features (background, padding, ribbons, and spacing) and three key defects (cracks, inactive areas, and gridlines).

Fig. 9 shows the distribution of precision and recall scores for each image and classification in the test dataset. Precision and recall are two common metrics used in machine learning to assess how well the model correctly classifies a pixel (precision) and how well the model locates a defect (recall). Values close to one indicate good agreement between the ground truth mask output from the manual inspection and the prediction mask output from the computer model. In general, precision and recall scored higher for features compared to defects, likely due to a higher pixel count for the features which cover a larger area of the image. The model performed equally well on both mono-si and multi-si cell images when detecting features, but performed better on mono-si when detecting defects. The improved performance on the mono-si cells may be a function of the larger sample size in the training dataset (69 mono-si vs 39 multi-si) and the smoother cell surface, without the grain boundaries visible on the multi-si cell images. Seven (7) cells with cracks were not detected at all, four mono-si cells and three multi-si cells. In these cells, the cracks were single lines that accounted for less than 0.2% of the pixels in the ground truth image and difficult for even a human expert to locate.

Fig. 10 shows the images associated with two cells from the test dataset. The original EL images were cropped from full module EL images. The ground truth masks were generated from the human inspection of the EL image. The prediction masks were generated by the trained u-net model based on the original EL image as input. A good machine learning model will reproduce the ground truth mask with high precision and recall, which should be a good representation of the original EL image, i.e. the ‘truth’. The prediction masks for these two solar cells demonstrate the potential for

semantic segmentation to generate reasonable estimates of the location, classification, and quantification of defects in EL images. The prediction mask is a numerical representation of the optical EL image with each pixel classified as one of the target defects, features, or background, which then enables large-scale statistical analysis of EL images on batches of full sized modules.

Fig. 11 shows the precision and recall matrices for the images shown in Fig. 10. These matrices quantify how well the prediction masks generated from the u-net model match the ground truth masks generated manually in GIMP. For example, the row labelled ‘inactive’ shows how well the computer model predicted the pixels that were labelled as ‘inactive’ in the ground truth mask. For image a), the matrices show that 80% of the pixels classified as ‘inactive’ by the computer model were also labelled ‘inactive’ in the ground truth image (precision), and 83% of the pixels labelled as ‘inactive’ in the ground truth mask were also labelled as ‘inactive’ in the prediction mask (recall). Similarly for image b), the row labelled as ‘cracks’ shows that 80% of the pixels labelled as ‘cracks’ by the computer model were also labelled ‘cracks’ in the ground truth mask (precision), and 73% of the pixels labelled as ‘cracks’ in the ground truth mask were also labelled as ‘cracks’ by the computer model (recall). A perfect computer model would show all ones along the diagonal.

The precision and recall metrics also depend on the quality of the ground truth masks, so accurate ground truth masks are critical for success. Fig. 12 shows the crack layer (white pixels) cropped from the center of Fig. 10a. The prediction mask is colored green. The remaining white pixels indicate cracks that were not detected by the model, thus contributing to low recall (48%). A closer inspection of this image also uncovered issues with the accuracy of the ground truth mask. In some regions, the computer-generated prediction mask was more accurate than the human-generated ground truth mask. Despite such errors, the u-net model does a reasonable job of identifying the cracks in the original EL image.

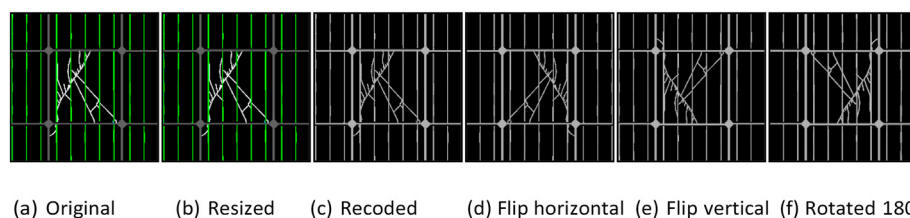


Fig. 8. Example showing the pre-processing of one original ground truth mask: a) original, b) resized, c) recoded, d) flipped horizontal, e) flipped vertical, and f) rotated 180° to produce four ground truth masks from each original (c,d,e,f) to effectively increase the size of the training dataset.

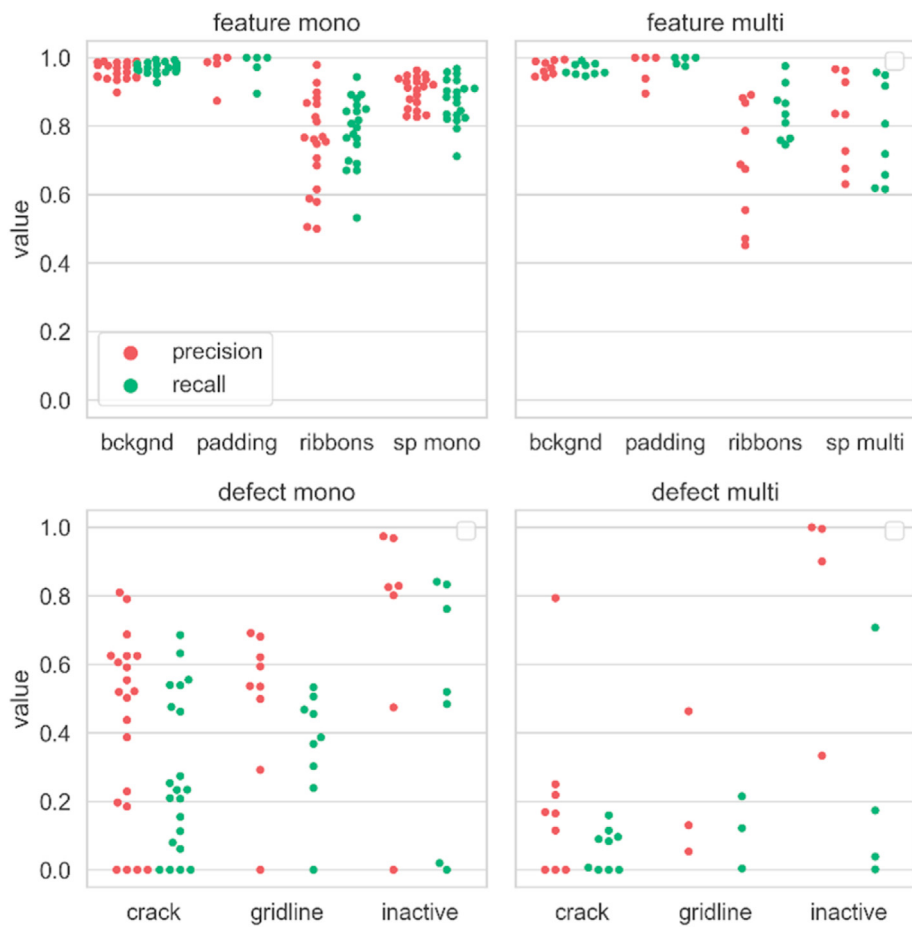


Fig. 9. Performance metrics for all images in the test dataset comparing the agreement between the ground truth mask output from the manual inspection and the prediction mask output from the computer model: precision and recall for thirty (30) test images.

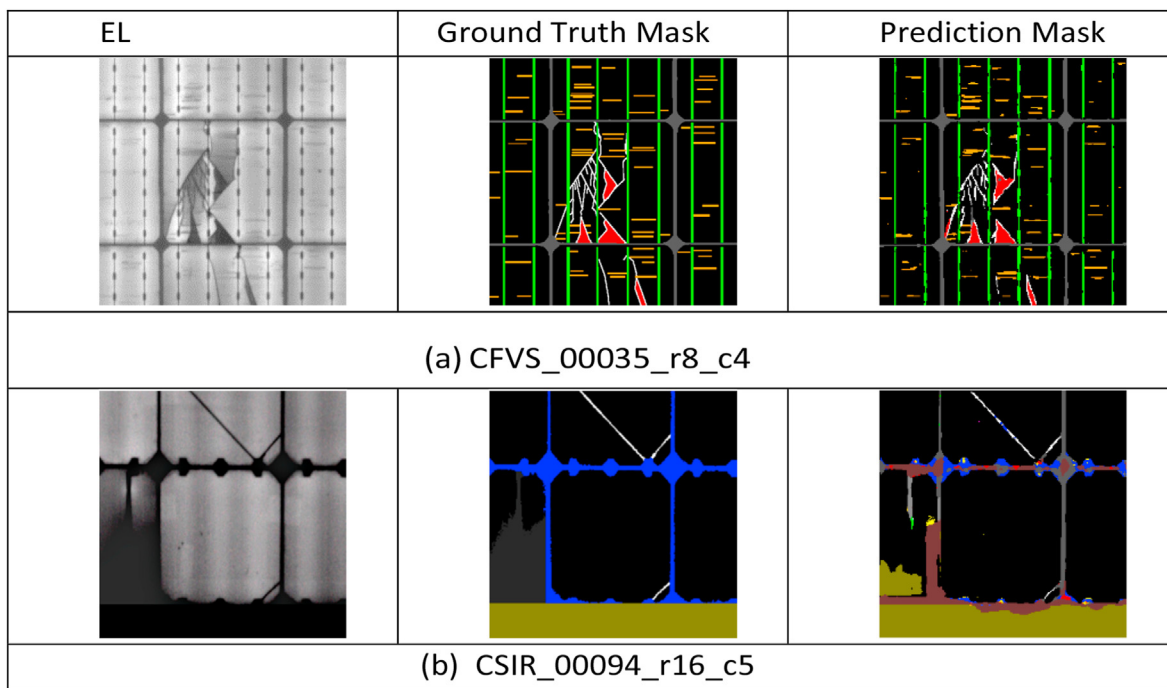


Fig. 10. Sample EL images cropped from the full module image (left), ground truth masks manually colored in GIMP (center), and the prediction mask output from the machine learning model (right) in which the colors correspond to different defects and features observed in the original EL image.

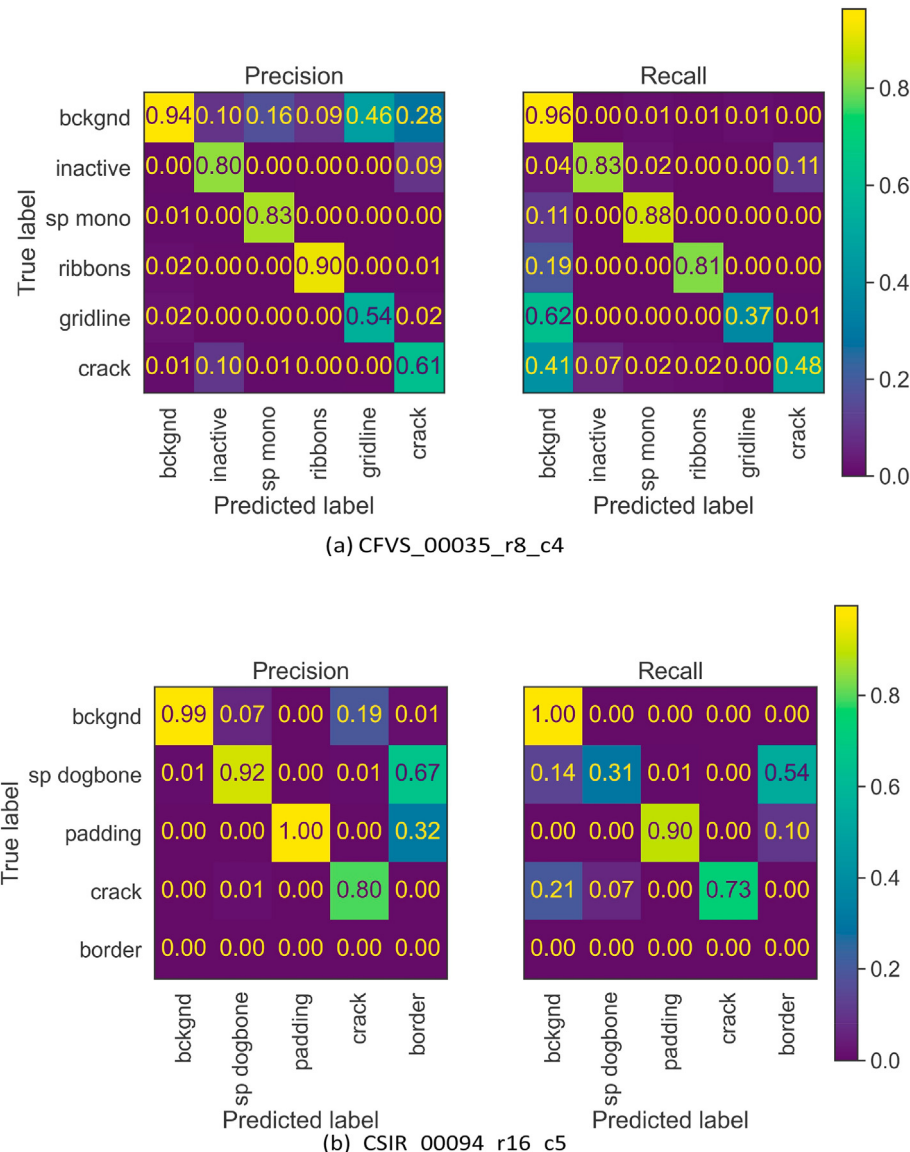


Fig. 11. Precision and recall matrices which quantify the ability of the computer model to reproduce the pixel colors manually labelled in the ground truth mask for two representative mono-si cells.

5.2. Model application for accelerated stress testing of PV modules

The trained u-net model can now be used to quantify changes in EL images over time or over a series of stress tests that are common in the PV industry during module certification and extended reliability testing. Fig. 13 shows the EL images from a single module run through a series of such tests at CFV Labs, including the static mechanical load test (SMLT), the dynamic mechanical load test (DMLT), thermal cycling (TC), and humidity freeze (HF). The HF10 indicates 10 HF cycles, and HF20 indicates 20 HF cycles. The SMLT results in cracks and inactive regions that did not appear in the initial EL image. The cracks can increase and lead to larger inactive regions by the end of this sequence. The prediction masks from the u-net model can be used to quantify the damage and correlate the electrical performance each stage of the accelerated stress test sequence.

Fig. 14 shows the EL images and computer-generated predictions masks for one cell cropped from the module-level images in Fig. 13. Specifically, this is the cell located on row 4 (r4) and

column 4 (c4). The EL images show substantial dendritic cracking after the SMLT, evolving into darker regions following the subsequent environmental stresses. The inactive regions become electrically isolated from the interconnect ribbons, meaning the current generated cannot be extracted from the solar cell and the electrical output of the module decreases. The prediction masks track the changes in the EL images as the cracks (white) evolve into inactive regions (red). However, the prediction mask is incorrectly predicting material defects (yellow) instead of correctly predicting inactive regions (red), especially in the last mage on the right.

Fig. 15 shows a similar set of images for another cell cropped from the module images in Fig. 13. This cell in row 8 and column 4 also shows significant dendritic cracking after the SMLT and similar evolution towards inactive regions following the HF stress. Again, the final image on the right shows a tendency to predict material defects (yellow) instead of inactive regions (red).

Fig. 16 shows another cell cropped from the same set of module images show in Fig. 13. In this cell from row 3 and column 2, singular cracks developed after SMLT rather than the dendritic cracks



Fig. 12. Crack layer for CFVS_00035_r8_c4 showing the prediction from the computer model (green) and the underlying ground truth mask manually colored (white) where the computer model failed to correctly label the pixels as cracks.

seen in the two previous cells. Smaller inactive regions evolve, and the corresponding red regions appear in the prediction masks. Gridline defects also developed at the edge of the long crack, seen as dark horizontal lines in the EL images. These defects correlate to the printed gridlines on the solar cell which are engineered to extract the current generated by the photovoltaic effect and carry it to the nearest interconnect ribbon. These gridline defects likely correlate to increased resistive losses, which leads to reduced electrical output from the PV module. Similar gridline defects appeared along some cracks in Figs. 14 and 15. However, the u-net model did a poor job of classifying these regions as gridline defects,

which appear as orange lines in the prediction masks.

Table 1 quantifies the change in pixel counts for the selected defect classes over the accelerated stress test sequence. The tabulated values show the number of pixels in each prediction mask shown in the figures above (16, 17, and 18). The pixel counts for cracks and inactive defects increased significantly post SMLT for all three cells, and the increase correlated to the changes observed in EL images. By the end of the accelerated stress sequence, the crack defect count decreased, and the inactive defect count increased relative to the post SMLT counts, as indicated by the ratio of post HF20 counts to the post SMLT counts shown in the rightmost column. This result is expected, as inactive regions tend to increase due to the thermal stresses in the real-world and induced in thermal cycling and humidity freeze [5]. However, the model did not capture the changes in gridline defects seen in the EL images, especially around the cracks post HF10 and post HF20. The row in the table labelled ‘noise’ represents the sum of the pixels wrongly classified into material (yellow), border (brown), and spacing multi (light gray) classes. The level of noise, or misclassification, tended to increase as the stress sequence progressed, especially for the two cells with dendritic cracks post SMLT.

6. Future work

The future work falls into two categories: improvements in the machine learning model and broader applications in PV modules. The machine learning aspect will focus on increasing the training dataset, improving the accuracy of the ground truth masks, and testing alternative neural networks to identify the best suited architecture for EL images. The future work in applications will focus on testing a completely different set of EL images from a new source and on the large-scale statistical analysis of different batches of modules.

7. Conclusion

A computer model based on semantic segmentation shows potential for detecting, classifying, and quantifying features and defects in EL images of PV modules made from mono- and multi-crystalline silicon cells. The model performed better on large intrinsic features such as cell spacing and ribbon interconnections compared to the smaller extrinsic defects such as cracks and gridline defects. The model performed better on the cells made from mono-si cells compared to cells made from the multi-si cells. The recall on inactive, crack, and gridline defects for cells made from mono-crystalline silicon wafers reached as high as 84%, 69%, and 53%, respectively. The output statistics from the model also correlated with changes observed in a sequence of EL images taken over several stages of an accelerated stress test experiment conducted at CFV Labs.

Semantic segmentation of EL images enables the quantification and large-scale statistical analysis of defects in millions of PV modules. Automation of the process fundamentally changes the amount and type of data that can be extracted from EL images, which opens opportunities for new analytics to correlate defects to electrical performance, compare module quality from different suppliers, and quantify changes in defect patterns over time. Semantic segmentation can also be applied to other renewable energy technologies because of the model's ability to convert any visual image to a numerical array that can be further analyzed by engineers and scientists in their respective fields to address other research questions and challenges.

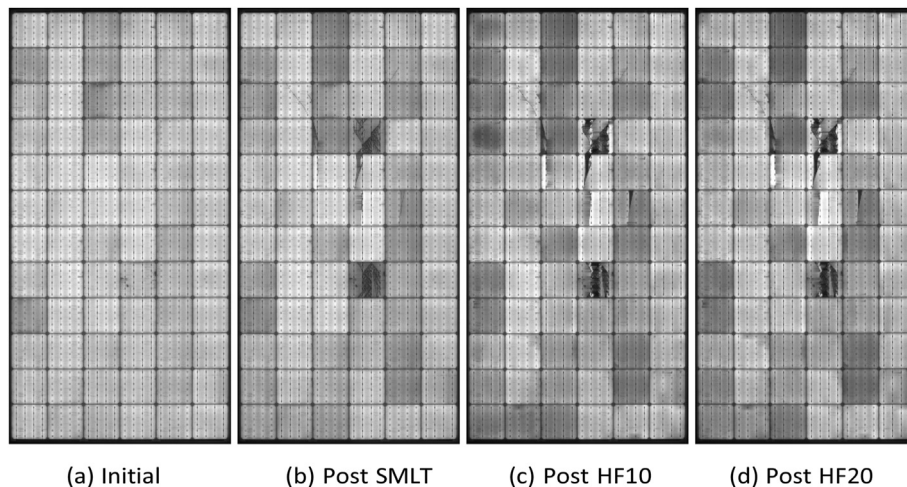


Fig. 13. EL images of a single module taken at several stages of an accelerated stress test sequence showing initial cells cracks after SMLT and gradual darkening of damaged areas with subsequent tests.

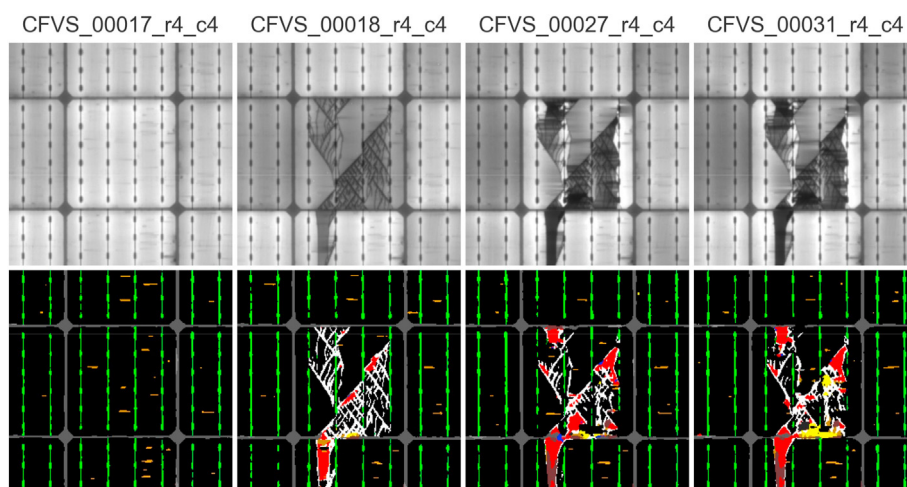


Fig. 14. Impact of accelerated stress testing as seen in the original EL images (top) and prediction masks from the U-Net model (bottom) for cell r4_c4 at initial, post SMLT, post HF10, and post HF20.

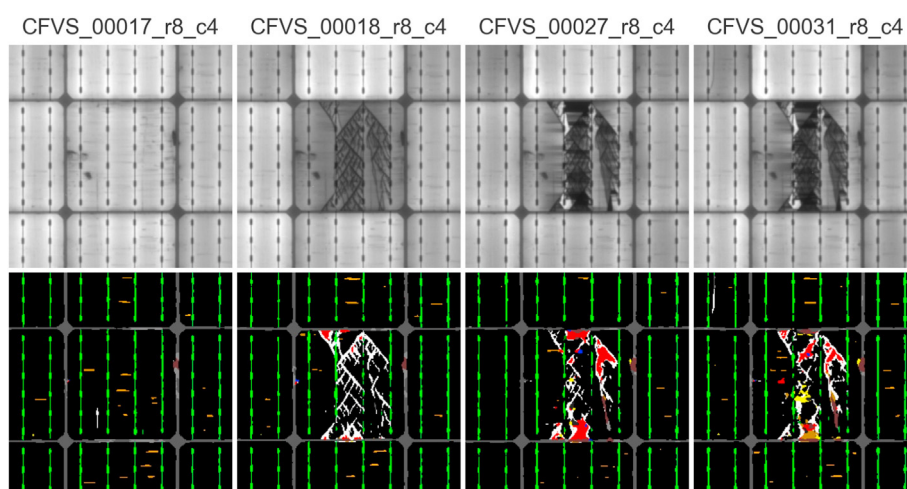


Fig. 15. Impact of accelerated stress testing as seen in the original EL images (top) and corresponding prediction masks from the u-net model (bottom) for cell r8_c4 at initial, post SMLT, post HF10, and post HF20.

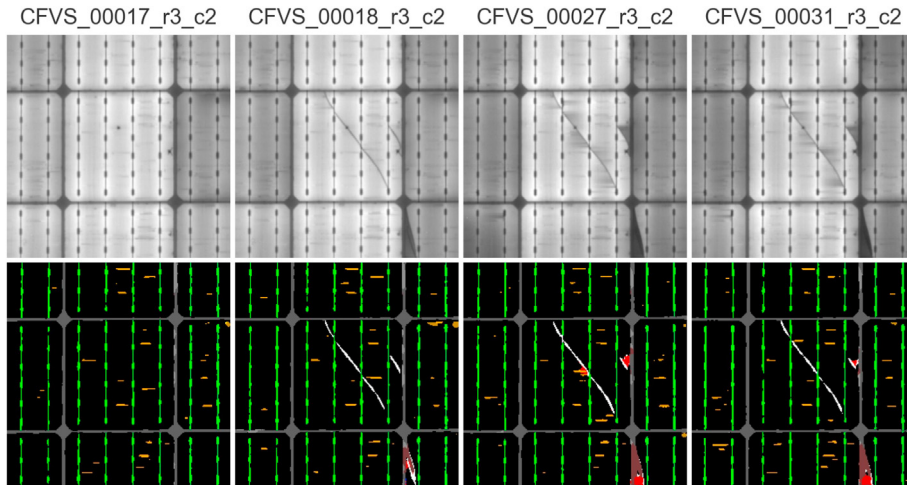


Fig. 16. Impact of accelerated stress testing as seen in the original EL images (top) and corresponding prediction masks from the u-net model (bottom) for cell r3_c2 at initial, post SMLT, post HF10, and post HF20.

Table 1

Pixel counts for predicted defect classifications during an accelerated stress test and the post HF20 to post SMLT ratio for three selected cells.

Desc	ID	Initial	Post SMLT	Post HF10	Post HF20	Ratio
crack	r4-c4	0	12184	7448	8040	0.66
	r8-c4	132	7428	4812	5996	0.81
	r3-c2	0	1304	1196	1108	0.85
inactive	r4-c4	0	2636	5932	5888	2.23
	r8-c4	8	640	3564	1864	2.91
	r3-c2	0	100	800	496	4.96
gridline	r4-c4	1040	752	808	684	0.91
	r8-c4	1044	668	360	808	1.21
	r3-c2	1244	1308	1376	1540	1.18
noise	r4-c4	432	756	3304	4052	5.36
	r8-c4	1908	1248	2148	3356	2.69
	r3-c2	904	2044	2392	2160	1.06

CRediT authorship contribution statement

Lawrence Pratt: Conceptualization, Methodology, Software, Validation, Formal analysis, Investigation, Resources, Data curation, Writing – original draft, Writing – review & editing, Visualization, Project administration, Funding acquisition. **Devashen Govender:** Software, Validation, Investigation, Data curation. **Richard Klein:** Conceptualization, Methodology, Formal analysis, Investigation, Resources, Writing – review & editing, Supervision, Project administration, Funding acquisition.

Declaration of competing interest

The authors declare that they have no known competing financial interests or personal relationships that could have appeared to influence the work reported in this paper.

Acknowledgments

The authors wish to thank Dr. Kittessa Roro and the CSIR for technical support, measurement equipment, test samples, and financial support for the PhD program that led to this publication. We wish to thank CFV Labs and ARTsolar for providing EL images and the team of labelers who annotated them: Nandi Bau, Sibusiso Mgidi, Rifumo Mzimba, Siyathandana Nontolwana, Kian Reddy, and Kyle Wootton from the University of the Witwatersrand; and Keketso Moletsane. This work is based on the research supported in

part by the National Research Foundation of South Africa (Grant Number: 118075).

References

- [1] G. Masson, I. Kaizuka, IEA PVPS trends in photovoltaic applications 2020.pdf. https://iea-pvps.org/wp-content/uploads/2020/11/IEA_PVPS_Trends_Report_2020-1.pdf, 2020.
- [2] M. Schmela, Global market outlook for solar power/2018–2022.pdf. <https://www.solarpowereurope.org/wp-content/uploads/2018/09/Global-Market-Outlook-2018-2022.pdf>, 2018.
- [3] Irena, Future of solar photovoltaic: deployment, investment, technology, grid integration and socio-economic aspects (a global energy transformation: paper).pdf. https://www.irena.org/-/media/Files/IRENA/Agency/Publication/2019/Nov/IRENA_Future_of_Solar_PV_2019.pdf, 2019.
- [4] R. Fu, D. Feldman, R. Margolis, M. Woodhouse, K. Ardani, US Solar Photovoltaic System Cost Benchmark: Q1 2017, Tech. Rep., EERE Publication and Product Library, 2017.
- [5] M. Köntges, I. Kunze, S. Kajari-Schröder, X. Breitenmoser, B. Bjørneklett, Quantifying the risk of power loss in pv modules due to micro cracks, in: 25th European Photovoltaic Solar Energy Conference, Valencia, Spain, 2010, pp. 3745–3752.
- [6] X. Qian, H. Zhang, H. Zhang, Y. Wu, Z. Diao, Q.-E. Wu, C. Yang, Solar cell surface defects detection based on computer vision, Int. J. Perform. Eng. 13 (7) (2017).
- [7] X. Qian, H. Zhang, C. Yang, Y. Wu, Z. He, Q.-E. Wu, H. Zhang, Micro-cracks detection of multicrystalline solar cell surface based on self-learning features and low-rank matrix recovery, Sensor Review 38-3 (2018) 360–368, <https://doi.org/10.1108/SR-08-2017-0166>.
- [8] M.D. Lydia, K.S. Sindhu, K. Gugan, Analysis on solar panel crack detection using optimization techniques, Journal of Nano-and Electronic Physics 9 (2) (2017), 2004–1.
- [9] S.A. Anwar, M.Z. Abdullah, Micro-crack detection of multicrystalline solar cells featuring an improved anisotropic diffusion filter and image segmentation technique, EURASIP Journal on Image and Video Processing 2014 (1) (2014) 15.
- [10] D.-M. Tsai, J.-Y. Luo, Mean shift-based defect detection in multicrystalline solar wafer surfaces, IEEE Transac- tions on Industrial Informatics 7 (1) (2010) 125–135.
- [11] C. Mantel, F. Villebro, G.A. dos Reis Benatto, H.R. Parikh, S. Wendlandt, K. Hossain, P. Poulsen, S. Spataru, D. Sera, S. Forchhammer, Machine learning prediction of defect types for electroluminescence images of photovoltaic panels, in: Applications of Machine Learning, vol. 11139, International Society for Optics and Photonics, 2019, p. 1113904.
- [12] A.M. Karimi, J.S. Fada, M.A. Hossain, S. Yang, T.J. Peshek, J.L. Braid, R.H. French, Automated pipeline for photovoltaic module electroluminescence image processing and degradation feature classification, IEEE Journal of Photovoltaics 9 (5) (2019) 1324–1335.
- [13] E. Sovetkin, A. Steland, Automatic processing and solar cell detection in photovoltaic electroluminescence images, Integrated Comput. Aided Eng. 26 (2) (2019) 123–137.
- [14] S. Deitsch, C. Buerhop-Lutz, A. Maier, F. Gallwitz, C. Riess, Segmentation of Photovoltaic Module Cells in Electroluminescence Images, 2018 arXiv preprint arXiv:1806.06530.
- [15] K.G. Bedrich, M. Bliss, T.R. Betts, R. Gottschalg, Electroluminescence imaging of pv devices: camera calibration and image correction, in: 2016 IEEE 43rd

- Photovoltaic Specialists Conference (PVSC), IEEE, 2016, pp. 1532–1537.
- [16] S. Spataru, P. Hacke, D. Sera, Automatic detection and evaluation of solar cell micro-cracks in electroluminescence images using matched filters, in: 2016 IEEE 43rd Photovoltaic Specialists Conference (PVSC), IEEE, 2016, pp. 1602–1607.
- [17] M.W. Akram, G. Li, Y. Jin, X. Chen, C. Zhu, X. Zhao, A. Khaliq, M. Faheem, A. Ahmad, Cnn based automatic detection of photovoltaic cell defects in electroluminescence images, Energy 189 (2019) 116319.
- [18] S. Deitsch, V. Christlein, S. Berger, C. Buerhop-Lutz, A. Maier, F. Gallwitz, C. Riess, Automatic classification of defective photovoltaic module cells in electroluminescence images, Sol. Energy 185 (2019) 455–468.
- [19] W. Tang, Q. Yang, K. Xiong, W. Yan, Deep learning based automatic defect identification of photovoltaic module using electroluminescence images, Sol. Energy 201 (2020) 453–460.
- [20] O. Ronneberger, P. Fischer, T. Brox, U-net, Convolutional networks for biomedical image segmentation, in: International Conference on Medical Image Computing and Computer-Assisted Intervention, Springer, 2015, pp. 234–241.
- [21] V. Badrinarayanan, A. Kendall, R. Cipolla, Segnet: a deep convolutional encoder-decoder architecture for image segmentation, IEEE Trans. Pattern Anal. Mach. Intell. 39 (12) (2017) 2481–2495.
- [22] H. Dong, G. Yang, F. Liu, Y. Mo, Y. Guo, Automatic brain tumor detection and segmentation using u-net based fully convolutional networks, in: Annual Conference on Medical Image Understanding and Analysis, Springer, 2017, pp. 506–517.
- [23] L.-C. Chen, Y. Zhu, G. Papandreou, F. Schroff, H. Adam, Encoder-decoder with atrous separable convolution for semantic image segmentation, in: Proceedings of the European Conference on Computer Vision (ECCV), 2018, pp. 801–818.
- [24] S. Cui, L. Mao, J. Jiang, C. Liu, S. Xiong, Automatic semantic segmentation of brain gliomas from mri images using a deep cascaded neural network, Journal of healthcare engineering 2018 (2018).
- [25] K. He, G. Gkioxari, P. Dollár, R. Girshick, Mask r-cnn, in: Proceedings of the IEEE International Conference on Computer Vision, 2017, pp. 2961–2969.
- [26] G. Roberts, S.Y. Haile, R. Sainju, D.J. Edwards, B. Hutchinson, Y. Zhu, Deep learning for semantic segmentation of defects in advanced stem images of steels, Sci. Rep. 9 (1) (2019) 1–12.
- [27] Y. Yuan, X. Chen, J. Wang, Object-contextual Representations for Semantic Segmentation, 2019, p. 11065, arXiv preprint arXiv:1909.
- [28] K. Zhang, Y. Zhang, H.-D. Cheng, Crackgan: pavement crack detection using partially accurate ground truths based on generative adversarial learning, in: IEEE Transactions on Intelligent Transportation Systems, 2020.
- [29] M. Köntges, S. Kurtz, C. Packard, U. Jahn, K.A. Berger, K. Kato, T. Friesen, H. Liu, M. Van Iseghem, J. Wohlgemuth, et al., Review of Failures of Photovoltaic Modules, 2014.
- [30] U. Jahn, M. Herz, M. Köntges, D. Parlevliet, M. Paggi, I. Tsanakas, Review on Infrared and Electroluminescence Imaging for PV Field Applications: International Energy Agency Photovoltaic Power Systems Programme: IEA PVPS Task 13, International Energy Agency, 2018. Subtask 3.3: report IEA-PVPS T13-12: 2018.
- [31] S. Johnson, T. Silverman, Photoluminescence and electroluminescence outdoor module imaging; nrel (national renewable energy laboratory), in: Tech. Rep., National Renewable Energy Lab.(NREL), Golden, CO (United States), 2015.
- [32] W.B. Hobbs, B. Hamzavy, C.B. Jones, C. Libby, O. Lavrova, In-field electroluminescence imaging: methods, comparison with indoor imaging, and observed changes in modules over one year, in: 2018 IEEE 7th World Conference on Photovoltaic Energy Conversion (WCPEC)(A Joint Conference of 45th IEEE PVSC, PVSEC & 34th EU PVSEC), IEEE, 2018, pp. 3257–3260.
- [33] M. Reuter, L. Stoicescu, J. H. Werner, PV Module Electroluminescence: Enlightening Defects 35. URL https://www.solarzentrum-stuttgart.com/uploads/file/platzhalter_vortrag_spezial_hagelschaden_DaySy_April2015_04.pdf.
- [34] M. Owen-Bellini, D.B. Sulas-Kern, G. Perrin, H. North, S. Spataru, P. Hacke, Methods for in situ electroluminescence imaging of photovoltaic modules under varying environmental conditions, IEEE Journal of Photovoltaics 10 (5) (2020) 1254–1261.
- [35] S. Koch, T. Weber, C. Sobottka, A. Fladung, P. Clemens, J. Berghold, Outdoor electroluminescence imaging of crystalline photovoltaic modules: comparative study between manual ground-level inspections and drone-based aerial surveys, in: 32nd Eur. Photovolt. Sol. Energy Conf. Exhib., 2016, pp. 1736–1740.
- [36] C. Buerhop-Lutz, S. Deitsch, A. Maier, F. Gallwitz, C. Brabec, A benchmark for visual identification of defective solar cells in electroluminescence imagery, in: 35th European PV Solar Energy Conference and Exhibition, vol. 12871289, 2018.
- [37] The GIMP Development Team, Gimp. URL <https://www.gimp.org>.
- [38] D. Gupta, image-segmentation-keras. <https://github.com/divamgupta/image-segmentation-keras>, 2020.